

# FAST AND SLOW RESPONSE MODES IN THE VENTILATION OF A LIVING COMPUTER LABORATORY

COSTANZA RODDA, GRAHAM O. HUGHES, AND JOHN CRASKE

**ABSTRACT.** We propose a dynamical systems approach to show how multi-zone models in buildings can be simplified upon recognising the existence of fast and slow modes of response. The study is motivated by extensive observations from an instrumented classroom equipped with 70 computers used heterogeneously in time and space – a living computer laboratory – that is mechanically-ventilated. We develop an analytical model for the  $\text{CO}_2$  evolution that accounts for air exchange between the classroom and ceiling plenum by parametrising the mixing of air within the sub-spaces, which is a feature that is often neglected in zonal models but shown to be essential for a realistic dynamical representation. We demonstrate how the model and interpretation of the data can be simplified by projecting the system onto a lower-dimensional subspace that describes the slow dynamics. This ability to reduce models based on a physical understanding is particularly valuable in the development of robust data-driven approaches. A comparison with the observational data demonstrates that the model is reasonably accurate in predicting  $\text{CO}_2$  concentrations in zones of ventilated spaces. Our laboratory offers a unique dataset to generate insights into the physics of realistic spaces containing non-uniform and time-varying heat sources, such as offices and classrooms. Observations show a remarkable seasonal change in mixing within the space, emphasising the importance mixing and temperature play in  $\text{CO}_2$  concentration.

## 1. INTRODUCTION

The COVID-19 pandemic and the unprecedented energy crisis Europe is facing demand that the construction sector maximise energy efficiency and simultaneously ensure a safe and comfortable environment for building occupants. Ventilation is recognised as an essential measure to reduce the risk of the indoor spreading of airborne infectious diseases, such as the SARS-CoV-2 virus [4, 7]. Following several studies assessing the effect of ventilation rates in reducing the infection probability of COVID-19 [9, 24], many countries have opted for increasing the running time of Heating, Ventilation, and Air Conditioning (HVAC) systems [11]. HVAC systems, however, are among the main contributors to a building’s life cycle carbon emissions and impact heavily upon a building’s running costs because they are associated with approximately 75% of the total energy consumption [14]. This study is inspired by the necessary reconciliation between the contrasting requirements for energy optimisation of ventilation systems and assuring occupants’ safety. One of the challenges we encounter in addressing this problem is related to the non-trivial behaviour of mechanically conditioned spaces. Indeed, the colder air emitted from air conditioners interacts with warmer air in the proximity of occupants. The resulting interplay between the thermal plume and the flow often assumes complex

patterns [27]. In some cases, local recirculation flows have increased the infection risk resulting in unusual spreads of COVID-19 in confined spaces [15].

Carbon dioxide ( $\text{CO}_2$ ) has been widely used as a proxy for ventilation and respiratory contaminants, starting from the pioneering work by Chaumont [8] in the 19th century. Later studies have connected  $\text{CO}_2$  measurements to the risk of transmission of respiratory diseases, including COVID-19 [21, 6, 20]. Measurements of indoor  $\text{CO}_2$  are easy to acquire via low-cost sensors that can be placed in rooms and have been used to monitor the risk of secondary infections via airborne transmission [26]. Furthermore,  $\text{CO}_2$  sources are relatively easy to quantify as they are correlated with the occupants. Considering also that transport of  $\text{CO}_2$  is limited to convection (or ventilation), its concentration field is more accessible to modelling than temperature, which is transported by convection, conduction, and radiation and whose sources are complicated to quantify.

A convenient way to represent the bulk evolution of  $\text{CO}_2$  in buildings is with nodal methods [10, 18]. In such models, each room is represented with a node and is modelled as being ‘well-mixed’, which means that a single value is used to characterise the bulk or mean  $\text{CO}_2$  concentration. More advanced ‘zonal’ models divide a space into a limited number of macroscopic subzones connected by interfaces through which airflow and heat are exchanged [16]. As air temperature is calculated in each subzone, these models can capture temperature distributions within a room. Although several aspects of the underlying sub-zonal physics are not included, zonal models improve the nodal models by providing a finer resolution representation of the problem.

In this paper, we adopt a dynamical systems approach to simplify the modelling of a multizone system. Specifically, we use the spectral properties of the system to identify fast and slow response timescales so that the evolution of  $\text{CO}_2$  concentrations can be projected onto a lower dimensional space. With the assumption that changes of the fast variables take place instantaneously, their role in the dynamical system becomes algebraic and determines a ‘slow manifold’ on which the remaining variables evolve. Such timescale separation has been investigated at length in different contexts, such as weather modelling [19], geophysical flows [25], and combustion chemistry [1]. Geometrically, we represent the evolution of the system as trajectories in phase space, which proves to be an insightful way of characterising the system’s behaviour.

Parker & Bowman [17] have applied a state-space formulation to study the analytical solutions and characterise the dynamical behaviour of multizone buildings in the context of contaminant transport. We adopt a similar approach, investigating the importance of eigenvalues in relation to the characteristics of our system. We examine a space composed of a plenum containing fan coil units above the suspended ceiling of the occupied room – a typical configuration for mechanically ventilated rooms. We consider such a configuration, which is relatively simple compared to other studies that consider multiple spaces, because our aim is to understand and model the air exchanges between the connected spaces and to parametrise mixing of the air within the sub-spaces.

The theoretical modelling is complemented with observational data from a ‘living’ laboratory – a highly instrumented classroom at Imperial College London. The laboratory is representative of a wide range of mixed ventilation spaces with characteristics encompassing many building types, including offices (with not less than 6

$\text{m}^2/\text{person}$ ), which are ubiquitous worldwide. The data measured in the laboratory serve not only as a validation for the model but also provide a way to understand how the system evolves in response to different configurations and forcings.

The laboratory, measurements, and dataset are introduced in §2, and the analytical model is described in §3. Section 4 focuses on comparing the model with the observed data, and our discussions and conclusions are given in §5 and §6.

## 2. A ‘LIVING’ LABORATORY AND DATASET

This study is based on data measured in a room equipped with many workstations (20.1 m in length, 8.0 m in width, and 3.2 m in height)—a ‘living’ laboratory—located at the South Kensington Campus of Imperial College London. Figure 1 shows a 3D sketch of the laboratory highlighting its main features. The laboratory is adjacent to a lecture room on the west side and an open-plan student space on the north and east sides. The south-facing facade has 12 double-glazed windows, each with a surface area of  $2.6 \text{ m}^2$  that are locked in a closed position. The laboratory is accessible through two doors located on the north wall. These doors are self-closing (and alarmed) and therefore open only for a small proportion of the time while people pass in and out of the room. The laboratory is subject to an extensive range of spatially and temporally heterogeneous thermal forcing; it hosts 70 workstations, a similar number of potential occupants, corresponding to floor space per person ranging from approximately 2 to  $160 \text{ m}^2$ , and is mechanically heated and cooled (see §2.1). The laboratory has been instrumented with numerous  $\text{CO}_2$ , humidity and temperature sensors throughout the room (see §2.3).

**2.1. Heating ventilation and air conditioning (HVAC).** The laboratory is mechanically ventilated via a typical Variable Air Volume (VAV) system controlled by a Building Management System (BMS). Temperature-controlled fresh air is pumped into a plenum above the room (see the green pipe in figure 1). Four Fan Coil Units (FCUs) (Quartz Sapphire model SPR9) draw air from the plenum and heat/cool the air using a hot/cold water system according to the temperature setpoint for the room. The conditioned air is ducted from the FCUs to supply the room via linear slot diffusers placed at the north and south sides of the room (blue pipes and arrows in figure 1). Air is extracted from the room through five square grilles positioned along the longitudinal axis of the ceiling (red pipes and arrows in figure 1) at a constant rate, which does not necessarily correspond to the rate at which air is supplied to the space by the FCUs.

**2.1.1. Air exchanges between the plenum and the room.** To account for the possible mismatch between the rate at which air is supplied by the FCUs and extracted according to the VAV system, the plenum and the room exchange air through two additional grilles on the ceiling (indicated as ‘ceiling grilles’ in figure 1). In addition, sections of the linear slot diffusers are not connected to the FCUs and allow air exchange between the room and the plenum. These air exchanges can occur in either direction (from the room towards the plenum and vice versa) depending on the AHU regime (the purple double arrows in figure 1 indicate the possible flow directions). Although the ceiling tiles are perforated, we expect that their acoustic insulation prevents significant flow.

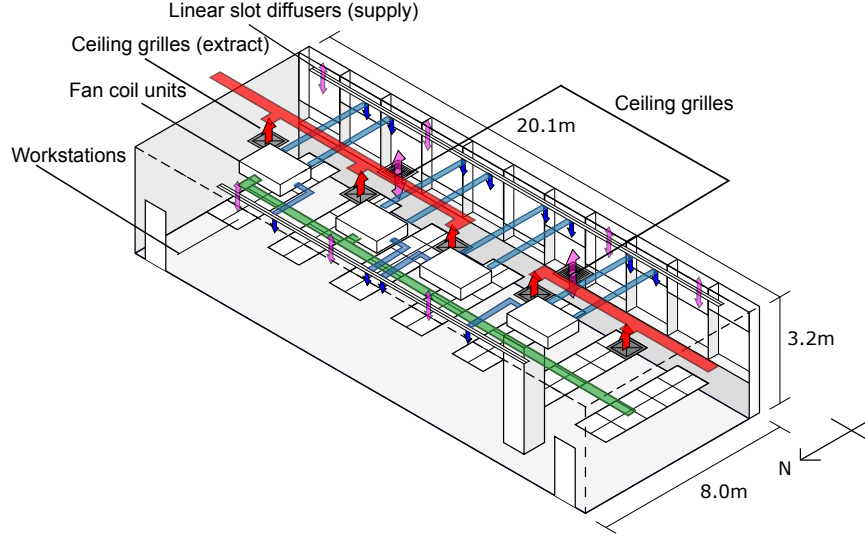


FIGURE 1. Schematic diagram of the laboratory. The coloured arrows indicate the airflow directions occurring at different ceiling locations. The blue arrows show the fresh air injected into the room by the four FCUs. The red arrows show the air extracted from the room through the five ceiling grilles. The purple double arrows show the air exchange pathways between the room and the plenum, i.e. through the additional two ceiling grilles and sections of the linear slot diffusers. The green pipe shows the temperature-controlled fresh air pumped towards the plenum. The red pipes show the air extraction circuit.

**2.2. Occupancy.** Occupancy information is inferred from Imperial’s deployment of the HubStar (formerly LoneRooftop) Building Insights Dashboard which infers occupancy from WiFi connections. The occupancy estimate is based on the number of users connected to the WiFi router in the room (hourly average and maximum values are recorded). Simma et al. [23] have reported that occupancy estimated from WiFi router data has an accuracy of 96%. High accuracy and easy availability make WiFi connections an excellent proxy for occupancy.

**2.3. Measurements.** The laboratory is monitored continuously with 24 temperature sensors (Trend thermistors model T/TFR 4) and 8 combined CO<sub>2</sub>/temperature/humidity sensors (TREND space sensors model RS-WMB-THC) connected to 4 Trend IQ4 controllers. The temperature sensors are installed on 4 vertical risers (i.e. 6 per riser) at different positions in the room. The combined sensors are situated on vertical walls at different horizontal positions in the room: vertical strings of 4 sensors on the interior column (figure 1) and of 2 sensors on the East wall, and either a vertical string of 2 sensors on the South wall or 1 sensor on the South wall and 1 sensor in the plenum of the room. The CO<sub>2</sub> and temperature measurements were further supplemented by sensors in the supply and extract ducting of the BMS system (§2.4).

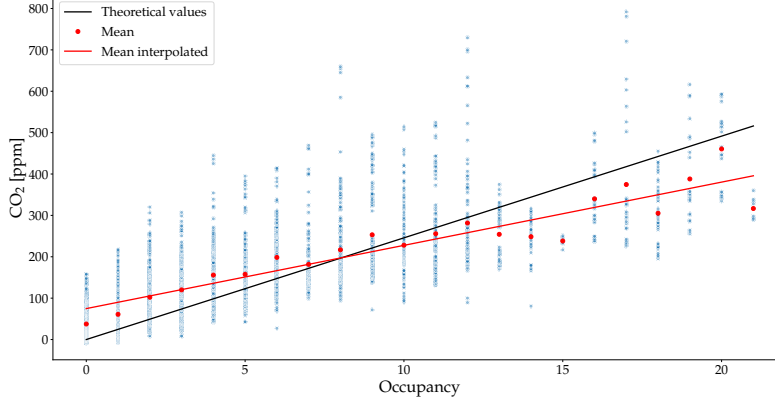


FIGURE 2. Excess  $\text{CO}_2$  concentration measurements from the sensors in the room versus the occupancy from data recorded in July 2022. The black straight line indicates the theoretical values of  $\text{CO}_2$  concentration from the steady state of the theoretical model. The red dots and line represent the measured data's mean and linear fit.

For the present study, we focus on the data provided by the 8 combined  $\text{CO}_2$ /temperature/humidity sensors. The dataset spans from January 2022 to September 2022, with measurements sampled and recorded every 5 minutes. We assume that the occupants are the only source of  $\text{CO}_2$  in the room, and figure 2 shows an example of the excess (relative to the environment) of  $\text{CO}_2$  concentration as a function of occupancy for July 2022. The  $\text{CO}_2$  concentration is based on an average of the 7 sensors placed in the room during this month, and the recorded room occupancy is based on the WiFi proxy. It can be seen that the  $\text{CO}_2$  concentration tends to increase with the occupancy, although a large spread is evident in the data. The solid black line indicates the theoretical values of  $\text{CO}_2$  concentration from the steady state of the theoretical model presented in §3.

**2.4. BMS.** We supplement the data acquired in the room with a range of measurements recorded by the BMS at 5-minute intervals. These measurements include the supply and extraction volume flow rates,  $Q_{\text{in}}$  and  $Q_{\text{out}}$ , respectively and the supply and return temperatures from the FCU. The flow rates  $Q_{\text{in}}$  and  $Q_{\text{out}}$  are measured by sensors placed in the air ducts. The data are presented in §4.

### 3. ANALYTICAL MODEL

**3.1.  $\text{CO}_2$  budget.** Let  $C_0$  and  $C_1$  be the bulk excess  $\text{CO}_2$  concentration (relative to outdoors) in the room and plenum, respectively, and let  $C'_0$  and  $C'_1$  be the quasi-steady state excess concentration associated with the ceiling zone and FCU, respectively (see figure 3 for a schematic representation of the spaces in a vertical cross-section of the room). We use  $q$  and  $q'$  to denote the rates at which fresh air is supplied and at which air is drawn into the plenum from the ceiling zone,

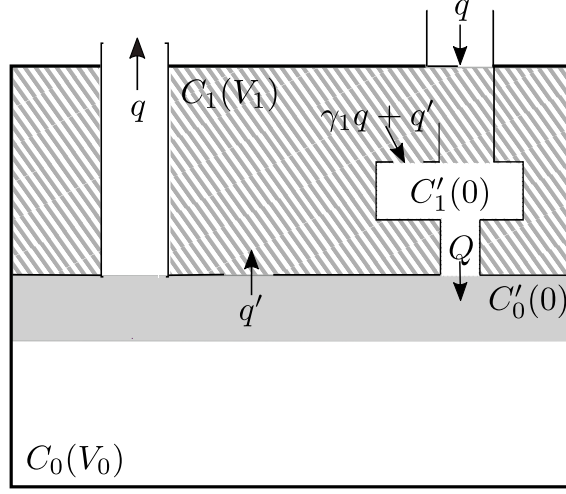


FIGURE 3. Schematic diagram of a vertical section of the room with the plenum on top (highlighted by the dashed pattern). The plenum has excess  $\text{CO}_2$  concentration  $C_1$  and volume  $V_1$ . The room excess concentration is indicated by  $C_0$ , and its volume is  $V_0$ .  $C'_1$  and  $C'_0$  indicate the excess  $\text{CO}_2$  concentrations in the FCU and ceiling zone (marked by the grey shaded area), respectively (see text for more details).

respectively, and define  $Q := q + q'$  (see figure 3). The variable  $Q$ , therefore, corresponds to the volume flux driven by the FCUs.

First, we establish an equation for the  $\text{CO}_2$  concentration in the FCUs, whose combined volume is labelled  $V'_1$ . Unless stated otherwise, all  $\text{CO}_2$  concentrations given henceforth refer to excess values.

Since the supply air duct is not connected directly to the FCUs, let  $\gamma_1 \in [0, 1]$  represent the fraction of the supply rate  $q$  that mixes with the air in the plenum:

$$(1) \quad V'_1 \frac{dC'_1}{dt} = \underbrace{(\gamma_1 q + q') C_1}_{\text{from plenum}} - \underbrace{Q C'_1}_{\text{to room}},$$

for which we have assumed that  $\gamma_1 q + q' \geq 0$ , which corresponds to the FCU always extracting air from the plenum.

For the control volume just below the room's ceiling, we adopt a similar approach to the FCU, using  $\gamma_0 \in [0, 1]$  to denote the fraction of FCU outlet air that mixes with the rest of the room:

$$(2) \quad V'_0 \frac{dC'_0}{dt} = \underbrace{\gamma_0 Q C_0}_{\text{from room}} + \underbrace{(1 - \gamma_0) Q C'_1}_{\text{from FCUs}} - \underbrace{q' \phi}_{\text{to plenum}} - \underbrace{q C'_0}_{\text{to extract}},$$

where

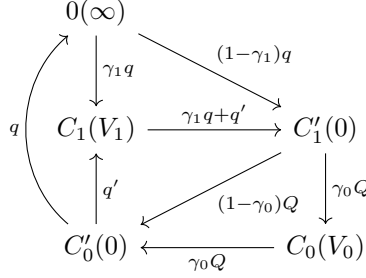


FIGURE 4. Network representation of the governing equations. The nodes represent control volumes (labelled with concentrations and volumes in parentheses) and the branches represent fluxes (labelled with volume fluxes).

$$(3) \quad \phi = \begin{cases} C'_0 & q' \geq 0, \\ C_1 & q' < 0, \end{cases}$$

allows the flux of CO<sub>2</sub> to be represented as either from the ceiling zone to the plenum ( $q' \geq 0$ ) or from the plenum to the ceiling zone ( $q' < 0$ ).

Let us now consider the CO<sub>2</sub> concentration in the room and plenum. We assume that both the plenum and the bulk of the occupied room are well mixed and that the rate of CO<sub>2</sub> generation per person is  $F$ . Furthermore, we assume that the infiltration and exfiltration of air are negligible (the validity of such an assumption is discussed in §4.1). The system of linear ODEs describing the time-variation of concentration in the room and the plenum, respectively, is therefore

$$(4) \quad V_0 \frac{dC_0}{dt} = \overbrace{\gamma_0 Q C'_1}^{\text{from FCU}} - \overbrace{\gamma_0 Q C_0}^{\text{to ceiling zone}} + NF,$$

$$(5) \quad V_1 \frac{dC_1}{dt} = \underbrace{q' \phi}_{\text{from ceiling zone}} - \underbrace{(\gamma_1 q + q') C_1}_{\text{to FCU}}.$$

The governing equations can be graphically represented in the network diagram in figure 4, where the nodes represent control volumes labelled with concentrations and their respective volumes in parentheses.  $0(\infty)$  represents the ambient, which is assumed to have infinite volume. The volume fluxes between control volumes are represented by the network's branches.

Let us now re-write the governing equations (1), (2), (4), and (5) in non-dimensional form by introducing the following variables:

$$(6) \quad \tau := \frac{q}{V_1} t, \quad \varepsilon := \frac{V_1}{V_0}, \quad \zeta := \frac{q'}{q}, \quad f_0 := \frac{NFV_1}{qV_0}.$$

Physically,  $\tau$  is a dimensionless time based on the filling time scale associated with the plenum (in terms of its volume  $V_1$  and the AHU supply volume flux  $q$ ),  $\varepsilon$  represents the ratio of the plenum and room volumes and  $\zeta$  is the ratio of the rates of room-plenum re-circulation and ambient fresh air introduction.

We further make the assumption that the volume of the FCUs and ceiling buffer zone are much smaller than the plenum volume, i.e.  $V_1'/V_1 \ll 1$  and  $V_0'/V_1 \ll 1$ . In physical terms, storage of  $\text{CO}_2$  in the FCU and ceiling buffer zone, accounting for the time derivative in (1)-(2) is therefore assumed to be unimportant, such that (1) and (2) give explicit algebraic expressions relating  $C_0'$  and  $C_1'$  to  $\gamma_0$ ,  $\gamma_1$ ,  $q$  and  $q'$ .

Under these assumptions, the resulting non-dimensionalised equations are

$$(7) \quad \frac{dC_0}{d\tau} = -\varepsilon\gamma_0(\zeta + 1)C_0 + \varepsilon\gamma_0(\zeta + \gamma_1)C_1 + f_0,$$

$$(8) \quad \frac{dC_1}{d\tau} = \zeta\phi - (\zeta + \gamma_1)C_1.$$

We can express the system (7) and (8) in the form

$$(9) \quad \frac{d\mathbf{C}}{d\tau} = \mathbf{A}\mathbf{C} + \mathbf{f}$$

where  $\mathbf{A}$  is a coefficient matrix,  $\mathbf{C} = (C_0, C_1)^\top$  is a state vector and  $\mathbf{f} = (f_0, 0)^\top$  is a forcing vector. Equation (9) can be converted into a homogeneous form by subtracting the steady-state solution from  $\mathbf{C}$ :

$$(10) \quad \mathbf{y} := \mathbf{C} + \mathbf{A}^{-1}\mathbf{f},$$

so that

$$(11) \quad \frac{d\mathbf{y}}{d\tau} = \mathbf{A}\mathbf{y} + \mathbf{A}^{-1}\frac{d\mathbf{f}}{d\tau},$$

where the second term on the right-hand side accounts for temporal changes in the forcing. Assuming that  $\mathbf{A}$  is diagonalisable (see discussion in §4.4 for the generalised case in which this assumption is not valid), let us now factorise  $\mathbf{A}$ :

$$(12) \quad \mathbf{A} = \mathbf{R}\mathbf{\Lambda}\mathbf{R}^{-1},$$

where  $\mathbf{\Lambda}$  is the eigenvalue matrix and  $\mathbf{R}$  is the corresponding (right) eigenvector matrix (explicit expressions for the matrices are given in A).

By substituting (12) into (11), premultiplying by  $\mathbf{R}^{-1}$  and defining

$$(13) \quad \mathbf{z} := \mathbf{R}^{-1}\mathbf{y},$$

equation (11) can be expressed in the simplified form

$$(14) \quad \frac{d\mathbf{z}}{d\tau} = \mathbf{\Lambda}\mathbf{z} + \mathbf{R}^{-1}\mathbf{A}^{-1}\frac{d\mathbf{f}}{d\tau},$$

where  $\mathbf{z}$  represents the amplitude of each eigenmode. If the forcing term  $\mathbf{f}$  is independent of time, then the system becomes autonomous:

$$(15) \quad \frac{d\mathbf{z}}{d\tau} = \mathbf{\Lambda}\mathbf{z},$$

and has the solution

$$(16) \quad \mathbf{z} = \mathbf{z}_0 \exp(\mathbf{\Lambda}\tau),$$

or, transforming back to the original coordinate system,

$$(17) \quad \mathbf{C} = \mathbf{R} \exp(\mathbf{\Lambda}\tau) \mathbf{R}^{-1} (\mathbf{C}_0 + \mathbf{A}^{-1}\mathbf{f}) - \mathbf{A}^{-1}\mathbf{f}.$$

Explicit expressions for the eigenvalues and eigenvectors are provided in A.



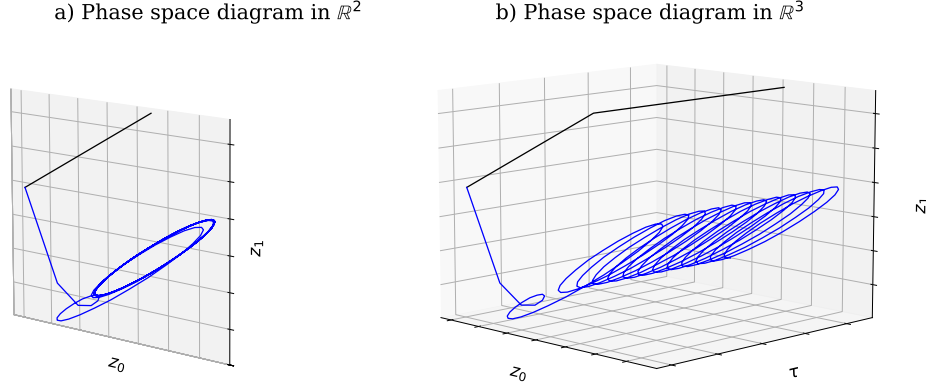


FIGURE 5. Example of phase space diagrams in  $\mathbb{R}^2$  (a) and in  $\mathbb{R}^3$  (b) for a forcing that is constant or periodic in time (black and blue line, respectively).

**3.2. Phase space diagrams.** Each possible state of the system is represented by a point in phase space. Lines in phase space trace the consecutive states that occur as the system evolves continuously in time. Therefore, phase space diagrams are a useful way to represent systems geometrically and investigate their equilibria, stability and evolution. For the autonomous system (15), the state evolution takes place on the phase space  $\mathbb{R}^2 \ni \mathbf{z}$  (see the plot in figure 5 (a)). Arrows in phase space therefore point in the direction in which  $\mathbf{z}$  changes with respect to time, according to (15). Trajectory lines of such a system join up the arrows and cannot cross each other because, for each  $\mathbf{z}$ , (14) defines a unique arrow direction.

For non-autonomous systems such as (14), phase space must be enlarged by one dimension (in such cases, time  $\tau$  is usually introduced as an additional ‘dependent’/state variable) to account for the fact that the two-dimensional phase portrait is affected by time-dependent forcing. Indeed, the trajectories corresponding to (14) would, in general, cross each other in  $\mathbb{R}^2$  because the right-hand side of (14) depends on time. In  $\mathbb{R}^3 \ni (\mathbf{z}, t)$ , however, trajectories corresponding to (14) do not cross (see figure 5 (b)). In this work, it will be convenient to plot states and trajectories with respect to the phase portrait corresponding to (15), acknowledging the possibility that the system’s trajectories may not be tangential to the arrows when  $d\mathbf{f}/d\tau \neq \mathbf{0}$ .

Figure 6 illustrates the solutions of (15), where the variable  $\mathbf{z}$  is expressed in terms of  $\mathbf{y}$  through (13) in phase space for fixed  $\varepsilon = 0.17$ ,  $\zeta = 1.8$ , and several combinations of  $\gamma_0$  and  $\gamma_1$  values. The values of  $\varepsilon$  and  $\zeta$  have been chosen as representative of the measurements in the living laboratory and are characteristic of a ventilated office space. The grey arrows in figure 6 mark flow evolution trajectories for different initial conditions.

The black dots show one particular solution of the dynamical system at uniform time intervals. They show that the solutions converge rapidly towards the equilibrium state  $\mathbf{y} = \mathbf{0}$ . The red and blue arrows mark the directions of the two

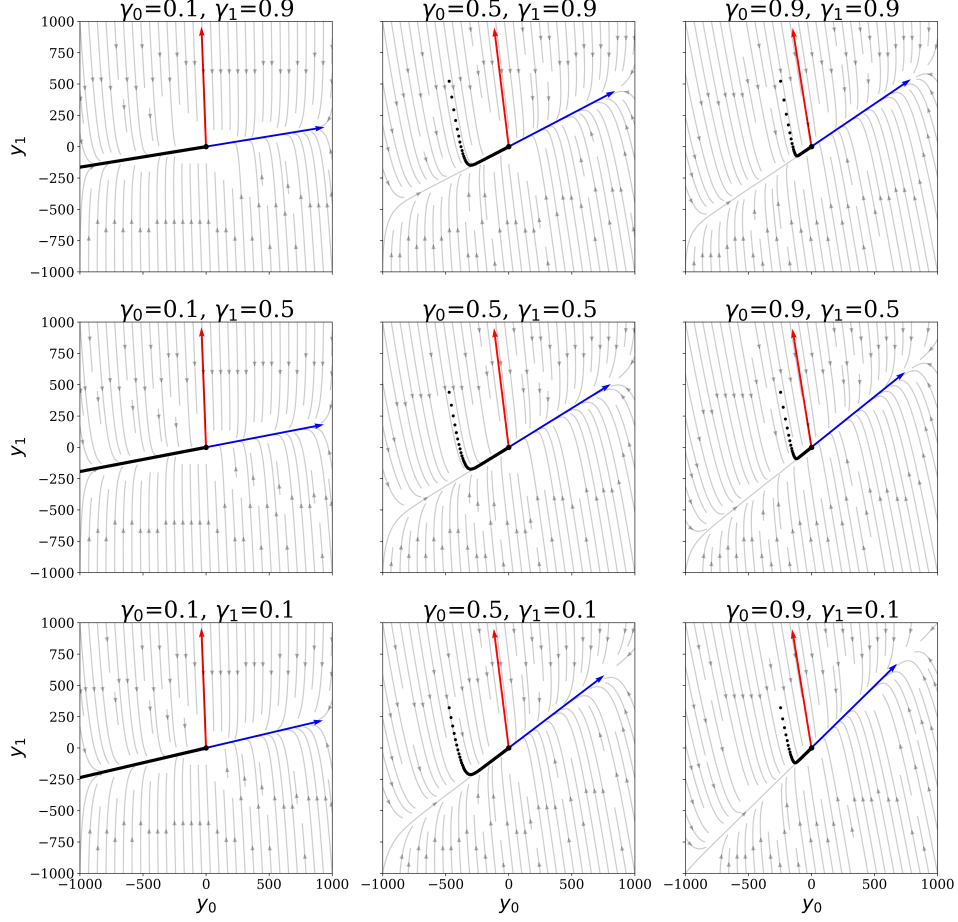


FIGURE 6. Phase space diagram corresponding to the variable  $\mathbf{y}$  (11) for fixed  $\varepsilon = 0.17$ ,  $\zeta = 1.8$ , and several combinations of  $\gamma_0$  and  $\gamma_1$  values. The grey arrows show the flow evolution trajectories for different initial conditions, and the black dots show one particular solution of the dynamical system at uniform time intervals. The equilibrium is subtracted from each data point. The red and blue arrows show the two eigenvectors.

eigenvectors and correspond to the fast (large negative eigenvalue) and slow (small negative eigenvalue) dynamics of the system, respectively.

In terms of the parameters, we can easily see that  $\gamma_1$  has far less influence on the dynamics than  $\gamma_0$ . This behaviour comes from the condition  $\varepsilon \ll 1$  ( $V_1 \ll V_0$ ). When  $\gamma_0 \rightarrow 1$  and  $\gamma_1 \rightarrow 0$ , the  $\text{CO}_2$  concentrations in the room and the plenum become comparable, as can be seen by the blue vector approaching a slope of one in the bottom right panel in figure 6. When  $\gamma_0 = 1$  and  $\gamma_1 = 0$ , the slow manifold lies onto  $y_0 = y_1$ , while the fast manifold corresponds to the difference between the  $\text{CO}_2$  concentration in the room and plenum. In all other cases, the concentration is higher in the room than in the plenum. The physical interpretation of slow and fast

Geometrical parameters		
Room volume	$V_0$	480 m <sup>3</sup>
Plenum volume	$V_1$	80 m <sup>3</sup>
Ratio of volumes	$\varepsilon = V_1/V_0$	0.17
Slot diffuser effective surface area: outlet	$A_{Lo}$	0.8 m <sup>2</sup>
Lateral linear slot diffuser effective surface area: inlet	$A_{Li}$	1.7 m <sup>2</sup>
Louvred face ceiling diffuser effective surface area	$A_{C1}$	0.14 m <sup>2</sup>
Grille ceiling diffuser effective surface area	$A_{C2}$	0.27 m <sup>2</sup>
BMS data (ON)		
Fresh air supply flow rate	$q_{in}$	$249 \pm 5 \text{ L s}^{-1}$
Return air flow rate	$q_{out}$	$236 \pm 5 \text{ L s}^{-1}$
BMS data (OFF)		
Fresh air supply flow rate	$q_{in}$	$7 \pm 2 \text{ L s}^{-1}$
Return air flow rate	$q_{out}$	$9 \pm 1 \text{ L s}^{-1}$
Average air speed		
Slot diffuser outlet	$v_{Lo}$	1 m s <sup>-1</sup>
Lateral linear slots inlet	$v_{Li}$	0.22 m s <sup>-1</sup>
Louvred face ceiling	$v_{C1}$	0.33 m s <sup>-1</sup>
Grille ceiling	$v_{C2}$	0.42 m s <sup>-1</sup>

TABLE 1. Geometrical parameters of the laboratory and volume fluxes measurements from BMS. The mean and standard deviations for the volume fluxes are calculated over a month of measurements. ON and OFF refer to the FCU being in operation or not, respectively.

manifold is less straightforward, as they can be identify in general as some linear combinations of the concentrations in the rooms, which depends on the mixing.

#### 4. DATA ANALYSIS AND COMPARISON WITH THE MODEL

This section is dedicated to analysing CO<sub>2</sub> data measured in the laboratory and comparing them with the predictions obtained from the model presented in §3.

**4.1. Volume flux budget.** We first analyse the data provided by the BMS and additionally consider air speed measurements taken in the room to estimate the air fluxes in the laboratory ( $q$ ,  $q'$ , and  $Q$ ) that are inputs for the model. The volume flux exchanges among the spaces in the laboratory can be schematically represented by the diagram in figure 4.

The rate of fresh air pumped into the room  $q$  is obtained by sensors placed in the supply and the return ducts recording the volume fluxes  $q_{in}$  and  $q_{out}$ , respectively (see values given in table 1). In the formulation of the analytical model, we assumed infiltrations and exfiltrations to be negligible; hence the supply air flux is equal to the return air flow rate. To verify whether such an assumption holds for the laboratory, we consider  $q_{in}$  and  $q_{out}$  data. Their mean values are given in table 1 for two regimes: when the FCU is in operation (ON) and when it is not (OFF). The FCU operates on weekdays between 8 am and 5 pm and is switched off

during the remaining times. During OFF, we can easily see that  $q_{\text{in}} \approx q_{\text{out}}$ . Hence the approximation holds. During ON, the difference between supplied and return air flux is  $\Delta q = q_{\text{in}} - q_{\text{out}} = 13 \text{ L s}^{-1}$ . Therefore, the room is slightly pressurised by the excess inflow. The error associated with the assumption  $q_{\text{in}} = q_{\text{out}}$  is 5%, which we can consider negligible for the purposes of this paper. To account for the difference, we verify whether the flux through the doors is consistent with the estimated leakage. Although the air volumes transported through open doorways can be large [13], the total time for which the doors are open is negligible. Therefore, we assume that the error associated with neglecting the open door flux is of the order of the measurement error ( $5 \text{ L s}^{-1}$  as in table 1). For closed doors, we measured the airspeed through the gaps surrounding the two doors, which is  $v_{\text{door}} = 0.44 \text{ m s}^{-1}$ . Considering the dimensions of the door frame and the few millimetres of space left between the door and the frame, we can estimate a volume flux  $\delta_{\text{door}} \approx 11 \text{ L s}^{-1}$ . Hence, the door leakage is enough to account for the slight imbalance between the supplied and return flux.

In addition to the volume fluxes provided by the BMS, we assess the recirculation volume flux  $q'$  and the FCU volume flux  $Q$  that are needed to solve the analytical system. Air exchanges between the upper room and the plenum mainly occur through two ceiling grilles (with effective surface areas  $A_{C1}$  and  $A_{C2}$  given in table 1) and the lateral linear slot diffusers (in the sections that are not connected to FCU outlet pipes, with effective surface area  $A_L$ , see table 1). Minor leaks of air can also occur through other small openings in the ceiling, which are not sealed, but we assume they are negligible compared to the main grilles. We measured the air velocity with an air transducer (TSI 8455-03 air velocity transducer, range 0.127 to 50.8 m/s with accuracy  $\pm 2\%$ ) at these main air exchange locations. Considering the airspeed and the effective surface areas, we estimate the flux by multiplying the velocity by the corresponding area through which the flow occurs. The flux estimates are:  $q_{Li} = 374 \text{ L s}^{-1}$  at the lateral linear slot diffusers, and  $q_{C1} = 46 \text{ L s}^{-1}$ , and  $q_{C2} = 113 \text{ L s}^{-1}$  through the ceiling grilles. These give

$$(18) \quad q' = q_{C1} + q_{C2} + q_{Li} \approx 545 \text{ L s}^{-1}.$$

If we consider the airspeed measured at the linear slot diffuser outlet, we estimate a flux from all four FCUs  $q_{Lo} = 800 \text{ L s}^{-1}$ . We can then verify that

$$(19) \quad Q = q + q' \approx 250 + 545 = 795 \text{ L s}^{-1}$$

is compatible with the measurements of  $q_{Lo}$ .

**4.2. Model and data comparison.** Figure 7 shows the measured excess of  $\text{CO}_2$  in the room ( $C_0$ ) and in the plenum ( $C_1$ ) for the entire month of July (weekends excluded) in a phase space diagram. The dataset is divided into two sets corresponding to the ON regime, in figure 7 (a) and to the OFF regime, in figure 7 (b). The model (in terms of the  $\mathbf{y}$  coordinate, see (11)) is also shown as a reference in plot a) (with the grey arrows marking the flow evolution trajectories and the red arrow marking the eigenvector representing the slow dynamics of the system). The forcing is set  $\mathbf{f} = 0$  in the model so that  $\mathbf{y} = \mathbf{C}$ . The volume fluxes and volumes are inputted into the model to form the matrix  $\mathbf{A}$  according to the measured values, while the parameters  $\gamma_0$  and  $\gamma_1$  cannot be measured and therefore need to be fitted with the data. For the case ON, the data are always well represented by  $\gamma_0 = 1$  and

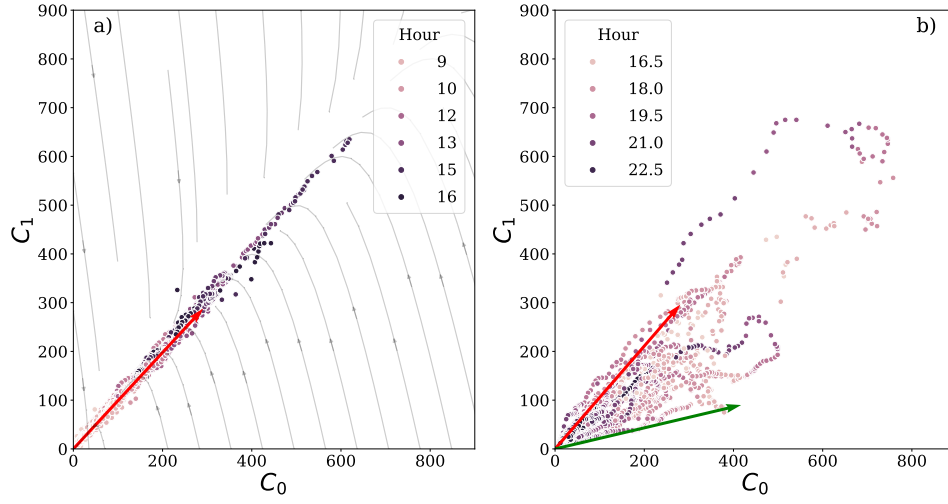


FIGURE 7. Phase space diagram showing the  $\text{CO}_2$  data in the room ( $C_0$ ) and in the plenum ( $C_1$ ) for July (excluding weekends). (a) data when ON, (b) data when OFF. The red arrow marks the eigenvector calculated for  $\gamma_0 = 1$  and  $\gamma_1 = 0$ , and the green arrow marks the eigenvector for  $\gamma_0 = 0.2$  and  $\gamma_1 = 0.5$

$\gamma_1 = 0$ . It is striking how the concentrations converge rapidly onto the subspace describing the slow dynamics of the system, marked by the red arrow. This points to a significant time separation between the slow and fast dynamics of the system. Another characteristic we can deduce from this plot is that the ventilation system could be considered as “overdriving” the response of the room in the sense that lower ventilation rates would still achieve a quick collapse onto the slow dynamics line.

In the OFF regime, the data are more scattered (figure 7 (b)). The data can be fit by the model for a range of  $\gamma$  parameters starting from the same conditions as in the ON regime (marked by the red arrow). The other data lie below such line and the model fit can be obtained by different combinations of  $\gamma_0$  and  $\gamma_1$ , suggesting that mixing both in the room and the plenum plays an important role in the OFF regime. In figure 7 (b), the green arrow marks the eigenvector calculated by setting  $\gamma_0 = 0.2$  and  $\gamma_1 = 0.5$ . However, similar eigenvectors can be obtained by setting  $\gamma_0 \leq 0.4$  and  $0 < \gamma_1 < 1$  (increasing  $\gamma_1$  compensates a decreasing  $\gamma_0$ ). As we have noticed previously,  $\gamma_1$  plays a minor role in determining the scattering of the data.

To better understand what causes the spread in the OFF regime, we plotted the phase space diagrams in figure 8 to compare the  $\text{CO}_2$  concentrations over six months, from June to November. The plots clearly show that during the warmer months (July, August, and September), the data are more spread, while in the colder months, they align along the eigendirection associated with the slow dynamics. Given the time of the year for which such differences appear, a reasonable explanation involves a link between the external temperature and the mixing inside

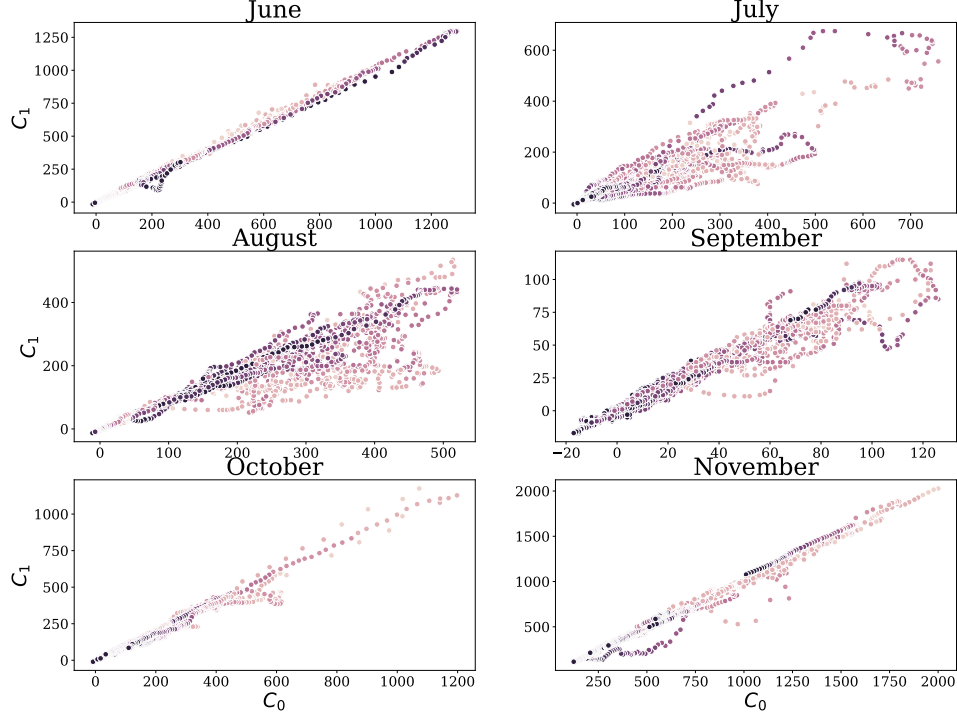


FIGURE 8. Phase space diagram showing the  $\text{CO}_2$  data in the room ( $C_0$ ) and the plenum ( $C_1$ ) for months between June 2022 and November 2022 at the times when the FCU is off.

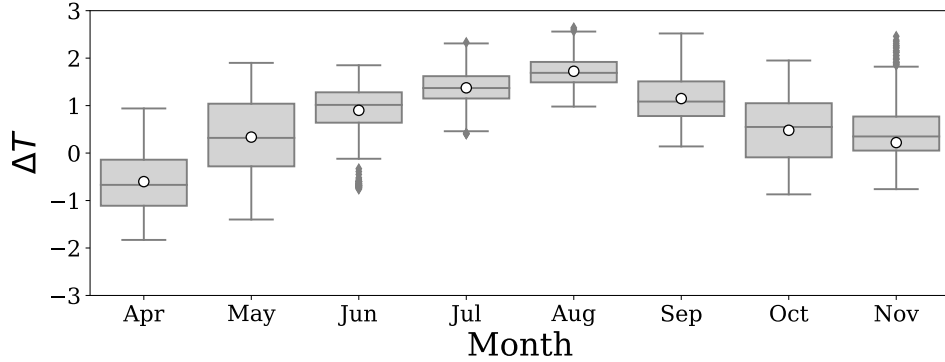


FIGURE 9. Boxplot of monthly averaged temperature difference between plenum and room. The horizontal line within each box marks the median, and the boxes extend from the first to the third quartile. The white dot marks the mean value. The diamonds shaped markers indicate the outliers.

the room and plenum. To demonstrate this link, we look at the difference in temperature recorded by BMS in the plenum and in the room, which show an increase

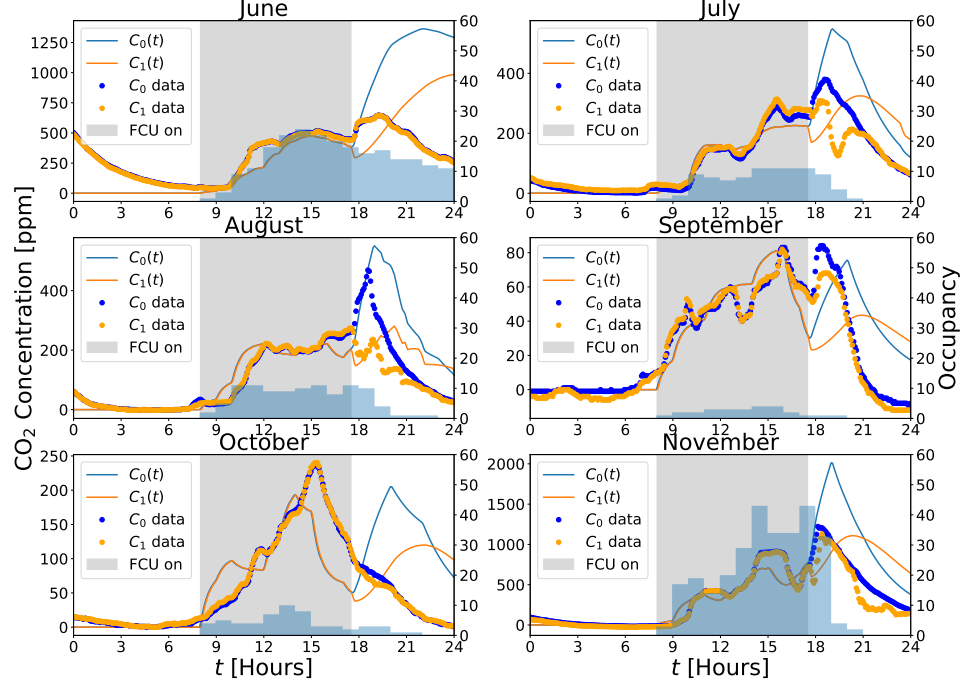


FIGURE 10.  $\text{CO}_2$  time evolution and model prediction. The data (blue and yellow dots) correspond to the measured concentrations in the laboratory on a representative day of the dataset (the first Tuesday of each month). The ambient  $\text{CO}_2$  (410 ppm) has been subtracted from the data. Note that the range of  $\text{CO}_2$  concentrations (left  $y$ -axis) differs significantly from month to month. The solid yellow and blue lines represent the solution of (7) and (8); see text for more details. The blue-shadowed histograms indicate occupancy in terms of the number of people in the room. The grey-shadowed region marks the ON regime.

in the temperature from the plenum to the room in the months of June, July, and August (see figure 9). During the warmer months, the external air supplied to the plenum is warmer than the air in the room. In this situation, the air transferred from the plenum into the room is warmer than that in the room. This lighter and warmer air enters the room through displacement, causing stratification along the vertical direction. On the contrary, when the air entering the room is colder, this heavier air descends readily, causing stirring and mixing. This analysis highlights that buoyancy-driven flow – whose effects are parameterised by the mixing parameter – might play an important role in determining the dynamics associated with  $\text{CO}_2$ .

Finally, we can use the theoretical model to study the time evolution of the  $\text{CO}_2$  within the room and the plenum. Figure 10 illustrates such a comparison for a chosen day (the second Tuesday for each month from June to November). The dataset spans very different conditions, with the occupation in any given hour ranging from a few people to over 50. The outside air temperature ranges from

a few degrees Celsius in the autumn months to above 30 degrees Celsius in the months of July and August.

The data (plotted in blue and yellow dots) corresponds to the  $\text{CO}_2$  concentrations in the laboratory. The solid yellow and blue lines represent the solution of (7) and (8).  $V_0$  and  $V_1$  are as given in table 1. The flux  $q = q_{\text{in}}$  has the values recorded by the BMS with a frequency of 5 minutes (the mean values for ON and OFF are given in table 1). The recirculation flux  $q'$  is assumed to be constant and equal to the value calculated from air speed measurements as explained in the previous section; hence  $q = 545 \text{ L s}^{-1}$  when ON, and when OFF  $q = q' = 7 \text{ L s}^{-1}$ . The forcing is calculated using the recorded occupancy from the WiFi data (see §2.2) multiplied by  $F = 0.012$ , which is the  $\text{CO}_2$  generation rate per person based on the level of physical activity for office workers [2]. The parameters  $\gamma_0$  and  $\gamma_1$  are set to  $\gamma_0 = 1$  and  $\gamma_1 = 0$  for the ON case, the latter indicating that the totality of the fresh air goes into the FCU without mixing with the air in the plenum. As discussed previously, the OFF case is more complex. In figure 10, we fixed the parameters to  $\gamma_0 = 0.2$  and  $\gamma_1 = 0.5$  for all the months for simplicity. However, more fine-tuning could be done by best fitting the data for each case.

Considering the uncertainty related to the occupancy estimation (see §2.2) and that occupancy is sampled only hourly whilst the data are sampled every 5 minutes, the model is in good agreement with the measurements, particularly for the regime ON. When the FCUs are on (in the shaded grey region of plot 10), the  $\text{CO}_2$  concentration in the room and the plenum are equal. On the contrary, when the FCUs are switched off, the  $\text{CO}_2$  response to the forcing is more unpredictable, and the difference between the concentrations in the plenum and in the room varies.

**4.3. Model reduction.** We revisit the model presented in §3.1, in light of the behaviour highlighted in the comparison with the measured data. What has emerged is that there are several situations in which there is a sufficiently large separation of timescales that, from the perspective of the relatively slow evolution of the overall system, the transient effects associated with the fast dynamics can be neglected. When the system is expressed in terms of  $\mathbf{z}$ , the approximation corresponds to assuming  $z_2 \approx 0$ . The simplification of physical systems by exploiting a separation of time scales in this way is used widely to derive low-dimensional dynamical systems and, in broad terms, corresponds to ‘adiabatic elimination’ of fast variables in stochastic systems [12].

If we consider the second component in (14)

$$(20) \quad \frac{dz_2}{d\tau} = \lambda_2 z_2 + \frac{1}{\lambda_2} R_{21}^{-1} \frac{df_0}{d\tau},$$

we can deduce that in order for the approximation  $z_2 \approx 0$  to be valid, the changes in the forcing need to occur slowly with respect to the fast time scale  $1/\lambda_2$ . If this condition is not satisfied, the system is two-dimensional, and the fast component cannot be considered zero. In practice, it could happen that the condition is not fulfilled when there are rapid changes in occupancy, such as at the beginning and end of a class.

By assuming that  $z_2 = 0$ , the reduced model can be written as

$$(21) \quad \frac{dz_1}{d\tau} = \lambda_1 z_1 + \frac{1}{\lambda_1} R_{11}^{-1} \frac{df_0}{d\tau},$$

and the solution (17) reduces to



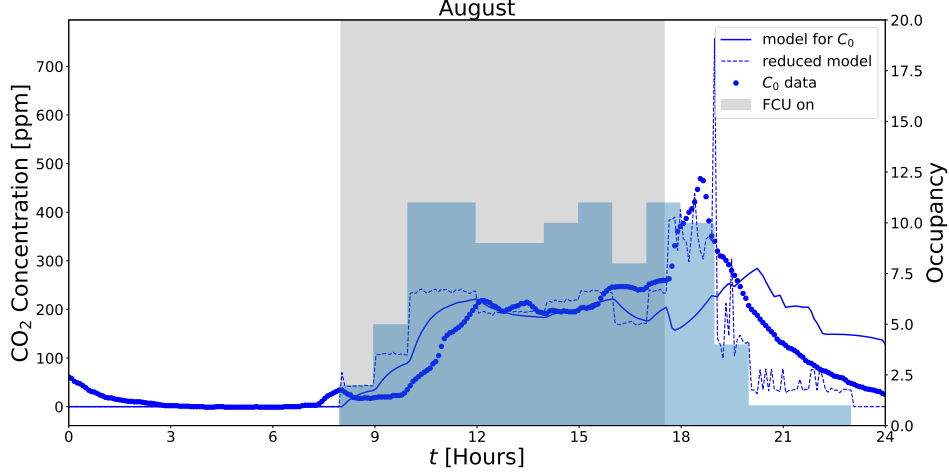


FIGURE 11. Comparison of the reduced (dashed line) and full model (solid line) with the observational data (dots) for the month of August. The parameters for the two models are the same as the one used in figure 8.

$$(22) \quad \mathbf{C} = \mathbf{R}_1 \exp(\lambda_1 \tau) \mathbf{R}_1^{-1} (\mathbf{C}_0 + \mathbf{A}^{-1} \mathbf{f}) - \mathbf{A}^{-1} \mathbf{f},$$

where  $\mathbf{R}_1$  is the column vector of the eigenvector matrix (corresponding to the two components of one eigenvector), and  $\mathbf{R}_1^{-1} := \mathbf{R}_1^\top / (\mathbf{R}_1^\top \mathbf{R}_1)$  is the left inverse. We can notice that (22) depends only on the eigenvalue and eigenvector associated with the slow dynamics.

The full and reduced models are compared in figure 11 (solid and dashed line, respectively), where the time evolution of  $C_0$  is plotted for a chosen day in August (same data as in figure 8). The reduced model prediction (given by (22)) is consistent with the full model prediction (given by the integration of (4)), even though the first is more affected by the coarse sampling of the forcing.

**4.4. Generalisation to larger dimensional models.** The model presented in §3.1 can be generalised to analyse the dynamics of multi-zone systems. Parker & Bowman [17] introduced an analytical approach to study the contaminant transport in multi-zone buildings. We follow a similar approach to briefly show here how our system can be expanded from 2-zones to any arbitrary  $n$ -zone configuration.

The matrix formulation used in §3.1 makes it straightforward to extend the model to the  $n$ -zones case. The system is expressed by (9), in which  $\mathbf{C}$  is now a vector of size  $n$ , and each  $C_i$  represents the  $\text{CO}_2$  concentration in a specific zone.  $\mathbf{A}$  becomes a  $n \times n$  matrix, the terms of which express how the  $\text{CO}_2$  transport occurs through connected zones. In general,  $\mathbf{A}$  cannot be diagonalised, but we can use the singular value decomposition (SVD), a matrix factorisation technique that is widely used to generalise the eigendecomposition [5]. The matrix  $\mathbf{A}$  can always be decomposed into  $\mathbf{A} = \mathbf{U} \mathbf{\Sigma} \mathbf{V}^*$ , where  $\mathbf{U}$  and  $\mathbf{V}$  are unitary matrices with orthonormal columns (\* indicates the complex conjugate transpose), and  $\mathbf{\Sigma}$  is a diagonal matrix of non-negative real numbers. The columns of  $\mathbf{U}$  and the columns

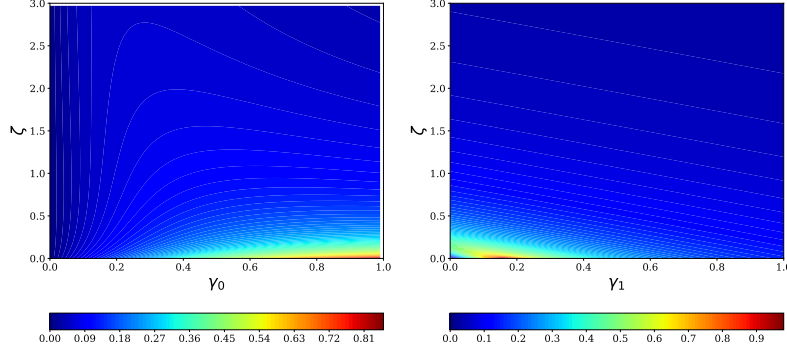


FIGURE 12. Ratio of eigenvalues (indicated by colour) as a function of the dependent variables  $\zeta$  and  $\gamma_0$  with  $\gamma_1 = 0.18$  (left), and  $\zeta$  and  $\gamma_1$  with  $\gamma_0 = 1$  (right).  $\varepsilon = 0.15$  for both panels.

of  $\mathbf{V}$  are called left-singular vectors and right-singular vectors of  $\mathbf{A}$ , respectively, and they form two sets of orthonormal bases. The diagonal elements of  $\mathbf{\Sigma}$  are called singular values, and it is always possible to choose a decomposition such that the singular values are in descending order.

Analogously to what we have done for the two-room system, analysing the singular vectors and singular values allows us to identify the most relevant properties of the system in a lower-dimensional space. The decision of how to reduce the original system, which in practice means determining how many singular values are necessary to describe the system, is somewhat arbitrary and problem-dependent. In the context of buildings, we have studied the evolution from initial conditions in very transient problems. The timescale analysis is useful to isolate fast from slow modes, which is therefore a suitable criterion for reducing the dimension of the system in the multi-zone case.

## 5. DISCUSSION

One striking characteristic emerging from the data analysis in §4.2 is the rapidity with which the  $\text{CO}_2$  concentration converges onto the slow dynamics of the system in the ON regime. In this case, we observe a dimensionality reduction of the system response, i.e. a collapse onto a single dimension. The resulting timescale separation between the fast and slow dynamics is more than a factor of 10: characteristic fast timescale is around 30 seconds while the slow timescale is above 5 minutes (characteristic timescales are calculated as  $1/\lambda$  and then dimensionalised as per (6)).

More generally, we can analyse the eigenvalues expressed in (29), which correspond to the magnitude of the corresponding eigenvectors, to identify possible reductions in the dimensionality of the dynamical system and predict for which configurations they occur. For  $\varepsilon \ll 1$ , the two eigenvalues are of a different order of magnitude throughout most of the parameter space, supporting characterisation by

a one-dimensional dynamical system. Regions where this approximation becomes invalid can also be found and depend on the values of the other three variables:  $\zeta$ ,  $\gamma_0$ , and  $\gamma_1$ . Figure 12 illustrates such dependencies for  $\varepsilon = 0.17$ . The ratio  $\max(\lambda_1, \lambda_2)/(\min(\lambda_1, \lambda_2))$  corresponds to the colours in the plot. As expected, for most of the parameter space, the one-dimensional reduction holds, with values of the ratio of the eigenvalues close to zero. If fresh air is introduced in the system, even a surprisingly small recirculation  $q' \gtrsim 0.3q$  is sufficient to promote collapse onto the one-dimensional system. However, for  $\zeta \lesssim 0.3$ , there are always combinations of  $\gamma_0$  and  $\gamma_1$  for which the system remains bi-dimensional.

The study of dimensionality reduction can be extremely helpful in understanding how the system works in different regimes and optimising its operational parameters, with a possible benefit in the cost and energy required to run the HVAC system. The estimation of the total energy consumption of an HVAC system is rather complex as it depends on a large number of variables, among which is the supply air flow rate [3]. Our analysis of this system has shown that the air supplied by the FCUs needs to generate a recirculation that is only 30% of the fresh air supplied into the plenum to optimise the  $\text{CO}_2$  concentration distribution between the room and the plenum. From this perspective, the excess air supplied to the room is overdriving the system without any real benefit in pollutant removal. Following the model suggestion, for the studied configuration, the FCU air supply could be reduced by more than half resulting in a significant reduction of costs without any impact on the air quality that occupants are subjected to. To give a rough estimation of the potential energy saving, halving the FCU flow rate would be expected to reduce the annual energy usage by 20-30% [22]. For a typical office space of similar dimension, this could lead to a decrease in the annual energy usage of 170 000 kWh (equivalent to  $1062 \text{ kW h m}^{-2}$ ).

## 6. CONCLUSIONS

We have developed an analytical model to study the evolution of  $\text{CO}_2$  concentration in connected spaces. The model validation with observational data has proved its robustness in predicting  $\text{CO}_2$  concentrations in sub-zones of ventilated spaces. We proposed an eigenmode decomposition of the model and analysed the properties in the phase space. The insights from this analysis have demonstrated the power of such an apparently simple algebraic methodology. In particular, it has enabled us to understand the evolution of the system based on some key parameters. For example, the ratio of volumes of the areas composing the system is fundamental as it characterises a time-scale separation in the dynamics with a consequent simplification of the problem and a dimensionality reduction. We have demonstrated the potential of this approach and how it can be expanded to any  $n$ -zone system, showing the potential to be incorporated into larger zonal models.

In the present study, we have focussed on introducing sub-volumes, but clearly, this is still a simplified model of the complex physics of buildings. Although the example proposed in the present study considers a relatively simple space, our model can be easily expanded to much more complicated configurations, as we have shown in section 4.4. When incorporated into larger zonal models, being able to reduce the dimensions of the resulting problem would prove even more valuable. One foremost future step is to include the spatial variability of the occupants. Localised sources of heat and  $\text{CO}_2$  impact the spatial distributions of the concentration, which

then affect the fluctuations that ultimately are overlooked in well-mixed models. Potential accumulation zones of  $\text{CO}_2$  are something to consider when planning where to place air extractors and could impact air quality and safety, which are of primary concern. The dataset available from our laboratory has the potential to answer some of the questions about spatial inhomogeneities thanks to the many sensors placed in the room at different locations.

## 7. ACKNOWLEDGEMENTS

This work was supported by the Engineering and Physical Sciences Research Council [grant number EP/V033883/1] as part of the [D\*]stratify project. We are grateful to Mark Reader for providing the BMS data and insightful comments about the HVAC system. We thank Neal Streamer and Trend Controls for supporting the project and providing the sensors and controllers. We thank Chris Banks from Imperial College London for facilitating access to the occupancy data from Imperial's deployment of the HubStar (formerly LoneRooftop) Building Insights Dashboard which infers occupancy from WiFi connections.

## APPENDIX A. SOLUTION OF THE $\text{CO}_2$ MODEL

We consider the eigenvalue matrix

$$(23) \quad \mathbf{\Lambda} = \begin{bmatrix} \lambda_1 & 0 \\ 0 & \lambda_2 \end{bmatrix}$$

and the block matrix

$$(24) \quad \mathbf{R} = \begin{bmatrix} v_1^{(1)} & v_1^{(2)} \\ v_2^{(1)} & v_2^{(2)} \end{bmatrix}$$

with the columns corresponding to each eigenvector  $\mathbf{v}_1 = (v_1^{(1)}, v_2^{(1)})$ ,  $\mathbf{v}_2 = (v_1^{(2)}, v_2^{(2)})$ . Let us consider a homogenous differential equation for which we want to calculate the eigenvalues  $\lambda$  and eigenvectors  $\mathbf{v}$

$$(25) \quad \mathbf{A}\mathbf{v} = \lambda\mathbf{v}$$

We can rewrite the system of non-homogeneous linear ODE of the first order in matrix form.

$$(26) \quad \frac{d}{dt} \begin{bmatrix} C_0 \\ C_1 \end{bmatrix} = \underbrace{\begin{bmatrix} \frac{-\gamma_0(q-Q)-\varepsilon}{V_0} & \frac{(q+\gamma_1 Q)+(1-\gamma_0)(q+\gamma_1 Q)}{V_0} \\ \frac{\gamma_0 q}{V_1} & \frac{(q\gamma_0+Q)(q+\gamma_1 Q)}{V_1(q+Q)} \end{bmatrix}}_A \begin{bmatrix} C_0 \\ C_1 \end{bmatrix} + \underbrace{\begin{bmatrix} NF \\ 0 \end{bmatrix}}_K.$$

We solve the homogenous differential equation by calculating the eigenvalues  $\lambda$  and eigenvectors  $\mathbf{v}$  such that

$$(27) \quad \mathbf{A}\mathbf{v} = \lambda\mathbf{v}$$

If we now look for a solution in the form

$$(28) \quad \begin{bmatrix} C_0 \\ C_1 \end{bmatrix} = A_0 \begin{bmatrix} v_1^1 \\ v_1^2 \end{bmatrix} \exp(\lambda_1 t) + B_0 \begin{bmatrix} v_2^1 \\ v_2^2 \end{bmatrix} \exp(\lambda_2 t).$$

For  $q' \geq 0$ , the eigenvalues are:

$$(29) \quad \lambda_{1,2} = \frac{1}{2(\zeta + 1)} \left[ -\varepsilon\gamma_0(1 + \zeta)^2 - (\gamma_1 + \zeta)(\gamma_0\zeta + 1) \pm S \right],$$

with

$$(30) \quad S = (-4\varepsilon\gamma_0(\zeta + 1)^2(\gamma_1 + \zeta) + ((\gamma_1 + \zeta)(\gamma_0\zeta + 1) + \varepsilon\gamma_0(\zeta + 1)^2)^2)^{\frac{1}{2}}$$

The eigenvalues are real, negative, and distinct. The eigenvectors are

$$(31) \quad \mathbf{v}_1 = \left[ -(\varepsilon\gamma_0(\zeta + 1)^2 - (\gamma_1 + \zeta)(1 + \gamma_0\zeta) + S_1), 2\gamma_0(\zeta + \zeta^2) \right],$$

and

$$(32) \quad \mathbf{v}_2 = \left[ -(\varepsilon\gamma_0(\zeta + 1)^2 - (\gamma_1 + \zeta)(1 + \gamma_0\zeta) - S_1), 2\gamma_0(\zeta + \zeta^2) \right],$$

with

$$(33) \quad S_1 = (\varepsilon^2\gamma_0^2(\zeta + 1)^4 + \varepsilon 2\gamma_0(\zeta + \gamma_1)(\zeta + 1)^2(\gamma_0\zeta - 1) + (\gamma_1 + \zeta)^2(1 + \gamma_0\zeta)^2)^{\frac{1}{2}}$$

The span of the two eigenvectors identifies a stable manifold.

## REFERENCES

- [1] AL-KHATEEB, A. N., POWERS, J. M., PAOLUCCI, S., SOMMESE, A. J., DILLER, J. A., HAUENSTEIN, J. D., AND MENGERS, J. D. One-dimensional slow invariant manifolds for spatially homogenous reactive systems. *The Journal of chemical physics* 131, 2 (2009), 024118.
- [2] ASTM, A. Standard d6245-18, standard guide for using indoor carbon dioxide concentrations to evaluate indoor air quality and ventilation1. *American Society for Testing and Materials. West Conshohocken, PA, USA* (2018).
- [3] ATTHAJARIYAKUL, S., AND LEEPHAKPREEDA, T. Real-time determination of optimal indoor-air condition for thermal comfort, air quality and efficient energy usage. *Energy and Buildings* 36, 7 (2004), 720–733.
- [4] BHAGAT, R. K., WYKES, M. D., DALZIEL, S. B., AND LINDEN, P. Effects of ventilation on the indoor spread of covid-19. *Journal of Fluid Mechanics* 903 (2020).
- [5] BRUNTON, S. L., AND KUTZ, J. N. *Data-driven science and engineering: Machine learning, dynamical systems, and control*. Cambridge University Press, 2022.
- [6] BURRIDGE, H. C., BHAGAT, R. K., STETTLER, M. E., KUMAR, P., DE MEL, I., DEMIS, P., HART, A., JOHNSON-LLAMBIAS, Y., KING, M.-F., KLYMENKO, O., ET AL. The ventilation of buildings and other mitigating measures for covid-19: a focus on wintertime. *Proceedings of the Royal Society A* 477, 2247 (2021), 20200855.
- [7] BURRIDGE, H. C., FAN, S., JONES, R. L., NOAKES, C. J., AND LINDEN, P. Predictive and retrospective modelling of airborne infection risk using monitored carbon dioxide. *Indoor and Built Environment* 31, 5 (2022), 1363–1380.
- [8] CHAUMONT, F. S. B. F. D. I. on the theory of ventilation: an attempt to establish a positive basis for the calculation of the amount of fresh air required for an inhabited air-space. *Proceedings of the Royal Society of London* 23, 156-163 (1875), 187–201.
- [9] DAI, H., AND ZHAO, B. Association of the infection probability of covid-19 with ventilation rates in confined spaces. In *Building Simulation* (2020), vol. 13, Springer, pp. 1321–1327.
- [10] DOLS, W. S., AND POLIDORO, B. *CONTAM user guide and program documentation: version 3.2*. US Department of Commerce, National Institute of Standards and Technology, 2015.
- [11] GUO, M., XU, P., XIAO, T., HE, R., DAI, M., AND MILLER, S. L. Review and comparison of hvac operation guidelines in different countries during the covid-19 pandemic. *Building and Environment* 187 (2021), 107368.
- [12] HAKEN, H. *Synergetics: An Introduction : Nonequilibrium Phase Transitions and Self-organization in Physics, Chemistry, and Biology*. No. v. 3 in Recent Results in Cancer Research. Springer, 1983.
- [13] JHA, N. K., FRANK, D., DARRACQ, L., AND LINDEN, P. Contaminant transport by human passage through an air curtain separating two sections of a corridor: Part ii—two zones at different temperatures. *Energy and buildings* 236 (2021), 110728.

- [14] LAUSTSEN, J. Energy efficiency requirements in building codes, energy efficiency policies for new buildings. *iea information paper*.
- [15] LIU, H., HE, S., SHEN, L., AND HONG, J. Simulation-based study of covid-19 outbreak associated with air-conditioning in a restaurant. *Physics of Fluids* *33*, 2 (2021), 023301.
- [16] MEGRI, A. C., AND HAGHIGHAT, F. Zonal modeling for simulating indoor environment of buildings: Review, recent developments, and applications. *Hvac&R Research* *13*, 6 (2007), 887–905.
- [17] PARKER, S., AND BOWMAN, V. State-space methods for calculating concentration dynamics in multizone buildings. *Building and Environment* *46*, 8 (2011), 1567–1577.
- [18] PARKER, S. T., LORENZETTI, D. M., AND SOHN, M. D. Implementing state-space methods for multizone contaminant transport. *Building and Environment* *71* (2014), 131–139.
- [19] PEÑA, M., AND KALNAY, E. Separating fast and slow modes in coupled chaotic systems. *Nonlinear Processes in Geophysics* *11*, 3 (2004), 319–327.
- [20] PENG, Z., AND JIMENEZ, J. L. Exhaled co2 as a covid-19 infection risk proxy for different indoor environments and activities. *Environmental Science & Technology Letters* *8*, 5 (2021), 392–397.
- [21] RUDNICK, S., AND MILTON, D. K. Risk of indoor airborne infection transmission estimated from carbon dioxide concentration. *Indoor air* *13*, 3 (2003), 237–245.
- [22] SANTOS, H. R., AND LEAL, V. M. Energy vs. ventilation rate in buildings: A comprehensive scenario-based assessment in the european context. *Energy and Buildings* *54* (2012), 111–121.
- [23] SIMMA, K. C. J., MAMMOLI, A., AND BOGUS, S. M. Real-time occupancy estimation using wifi network to optimize hvac operation. *Procedia Computer Science* *155* (2019), 495–502.
- [24] SUN, C., AND ZHAI, Z. The efficacy of social distance and ventilation effectiveness in preventing covid-19 transmission. *Sustainable cities and society* *62* (2020), 102390.
- [25] VANNESTE, J. Balance and spontaneous wave generation in geophysical flows. *Annual Review of Fluid Mechanics* *45* (2013), 147–172.
- [26] VOURIOT, C. V. M., BURRIDGE, H. C., NOAKES, C. J., AND LINDEN, P. F. Seasonal variation in airborne infection risk in schools due to changes in ventilation inferred from monitored carbon dioxide. *Indoor Air* *31*, 4 (Jul 2021), 1154–1163.
- [27] XI, H.-D., LAM, S., AND XIA, K.-Q. From laminar plumes to organized flows: the onset of large-scale circulation in turbulent thermal convection. *Journal of Fluid Mechanics* *503* (2004), 47–56.